J Comput Electron (2007) 6:305–308
DOI 10.1007/s10825-006-0117-3

Monte Carlo modeling of X-valley leakage in quantum cascade lasers

Xujiao Gao · Dan Botez · Irena Knezevic

Published online: 18 January 2007

Abstract This paper presents the first comprehensive Monte Carlo simulation of GaAs/AlGaAs quantum cascade lasers (QCLs) that takes both Γ- and X-valley transport into account and investigates the effect of X-valley leakage on the QCL performance. Excellent agreement with experimental data is obtained for the GaAs/$Al_{0.45}Ga_{0.55}$As QCL at cryogenic and room temperatures. The model reveals two carrier-loss mechanisms into the X valley: coupling of the Γ continuum-like states with the X states in the same stage, and coupling between the Γ localized states in the simulated stage with the X states in the next stage. Simulation results demonstrate that the 45% Al QCL has small X-valley leakage at both 77 K and 300 K, due to the very good confinement of the Γ states, stemming from the high Al content.

Keywords Quantum cascade lasers · Monte Carlo · X-valley leakage · Intervalley scattering

1 Introduction

Room-temperature, pulsed mode operation of a 9 μm GaAs/AlGaAs intersubband quantum cascade laser (QCL) has been accomplished by increasing the Al content from 33% to 45% within the conventional three-well active region design [1]. This important milestone in the mid-infrared (mid-IR) GaAs/AlGaAs QCL technology was achieved due to the ∼80 meV larger band offset in the 45% Al structure than the GaAs/$Al_{0.33}Ga_{0.67}$As QCL [2], which suppressed thermal leakage into the Γ-valley continuum-like states and significantly improved the temperature dependence of the threshold current density [3]. However, GaAs/AlGaAs QCLs with Al content of above 45% show worse performance than the 45% QCL in experiment [4], which was believed to be due to intervalley scattering. Satellite-valley leakage can also play a significant role in carrier loss in InP-based mid-IR QCLs [5], especially at high fields and high temperatures. Therefore, it has become a necessity to incorporate both Γ- and satellite-valley transport into theoretical QCL modeling, while the published theoretical models have so far focused on the Γ-valley electronic transport only [6–8].

In this paper, we present the first comprehensive Monte Carlo simulation [9] of the well-known GaAs/$Al_{0.45}Ga_{0.55}$As QCLs [1] (referred to as 45% QCL) that takes both Γ-valley and satellite-X-valley transport into account. The 3D Monte Carlo QCL simulator we developed is based on solving the microscopic Boltzmann-like transport equation of Ref. [7], with the X-valley transport incorporated. The effect of X-valley leakage on the performance of the 45% QCL is investigated at various applied fields and temperatures. Simulated threshold current density with the X-valley leakage is in excellent agreement with experiment at both cryogenic (77 K) and room temperatures. The simulation reveals two mechanisms of carrier loss into the X valley: coupling of the Γ continuum-like states with the X states in the same stage, and coupling between the Γ localized states in the simulated stage with the X states in the next stage. The 3D Monte Carlo QCL model is elaborated in Section 2, and the

X. Gao (✉) · D. Botez · I. Knezevic
Department of Electrical and Computer Engineering, University of Wisconsin, Madison, 1415 Engineering Dr, Madison, WI 53706-1691, USA
e-mail: xujiaogao@wisc.edu

D. Botez
e-mail: botez@engr.wisc.edu,

I. Knezevic
e-mail: knezevic@engr.wisc.edu

simulation results are presented and discussed in Section 3, followed by a conclusion in Section 4.

2 3D Monte Carlo model

Quantum cascade laser is a complex multi-quantum-well (MQW) structure consisting of repeated identical stages (typically 25–70), each containing the active region sandwiched between the electron-injecting and -collecting regions. Stationary electronic transport in mid-IR QCLs is incoherent and the electron distribution $f_{\mathbf{k}\alpha}$ in each stage (active region and injector/collector) evolves according to the Boltzmann-like equation [7, 8]:

$$\frac{d}{dt} f_{\mathbf{k}\alpha} = \sum_{\mathbf{k}'\alpha'} [P_{\mathbf{k}'\alpha',\mathbf{k}\alpha} f_{\mathbf{k}'\alpha'}(1 - f_{\mathbf{k}\alpha}) - P_{\mathbf{k}\alpha,\mathbf{k}'\alpha'} f_{\mathbf{k}\alpha}(1 - f_{\mathbf{k}'\alpha'})], \quad (1)$$

where $|\,\mathbf{k}\alpha\rangle = |\,\mathbf{k}, \nu\lambda\rangle$ denotes the 3D single-particle electronic state in the λth stage, νth Γ-valley subband, and with the in-plane wave vector $\mathbf{k}$. To incorporate the electronic transport in other valleys (e.g., the X valley in GaAs/AlGaAs QCLs) into the model, we extend the state $|\,\mathbf{k}, \nu\lambda\rangle$ to $|\,\mathbf{k}, \nu_\ell\lambda\ell\rangle$, with the valley index ℓ as the fourth quantum number and ν_ℓ counting subbands in the ℓth valley. $P_{\mathbf{k}'\alpha',\mathbf{k}\alpha}$ is the total transition rate from state $|\,\mathbf{k}'\alpha'\rangle$ to $|\,\mathbf{k}\alpha\rangle$, written as $P_{\mathbf{k}'\alpha',\mathbf{k}\alpha} = \sum_s P^s_{\mathbf{k}'\alpha',\mathbf{k}\alpha}$, with the sum over all possible scattering mechanisms s. Each transition rate $P^s_{\mathbf{k}'\alpha',\mathbf{k}\alpha}$ is calculated using Fermi's Golden Rule.

The translational symmetry of QCL structures (i.e., the wave functions in any two stages are simple translations in space and energy) allows us to simulate carrier transport over a 'central' stage λ only [7, 10]. Spatially remote stages have little wavefunction overlap with the central-stage wavefunctions, making it sufficient to limit the interstage scattering ($\lambda' \neq \lambda$) to just the nearest-neighbor stages ($\lambda' = \lambda \pm 1$). Calculation of all the intrastage ($\lambda' = \lambda$) and the nearest-neighbor interstage ($\lambda' = \lambda \pm 1$) transition rates requires the knowledge of energy levels/wave functions in two full adjacent stages.

The Γ-valley states in two adjacent stages are obtained by solving the 1D Schrödinger equation in the growth direction (z-axis) using the three-band $\mathbf{k}\cdot\mathbf{p}$ method within the envelope function framework, while the in-plane state is approximated by a plane wave. The three-band $\mathbf{k}\cdot\mathbf{p}$ technique simultaneously solves for the envelope functions and energy levels of the conduction, light-hole, and spin-orbit split-off bands. Moreover, the $\mathbf{k}\cdot\mathbf{p}$ method can easily incorporate the effect of strain which occurs in some QCL structures. The self-consistent band bending owing to the actual charge distribution in the QCL is not accounted for, as its effect on the electronic states has been proven negligible for the conventional doping level of 3.9×10^{11} cm^{-2} [11].

As for the X-valley (three X valleys in the first Brillouin zone) states, the usual effective-mass equation is sufficient, since the X valleys are well above the valence bands and the subband mixing is negligible. The longitudinal effective mass m^*_l is used in the effective-mass equation for the X valley whose longitudinal direction is along the growth direction ([001] growth is assumed), denoted as $X1$ valley, while the transverse m^*_t is used for other two X valleys whose longitudinal directions are in the plane (x-y plane) perpendicular to the growth direction, denoted as $X2$ valleys. The effective-mass equations for the three X valleys are solved simultaneously in the reciprocal space [12]. The resulting subbands form a nondegenerate set (longitudinal) corresponding to the $X1$ valley, and a doubly-degenerate set (transverse) corresponding to the two $X2$ valleys. The in-plane effective masses of Γ- and X-valley subbands are then recalculated employing the full subband wave functions (they are not taken to be the same as in either bulk material), and a parabolic approximation with that accurate in-plane mass is utilized in the Monte Carlo transport kernel.

Figure 1 illustrates the electronic structure of the 45% QCL in two adjacent stages at $F = 55$ kV/cm (above

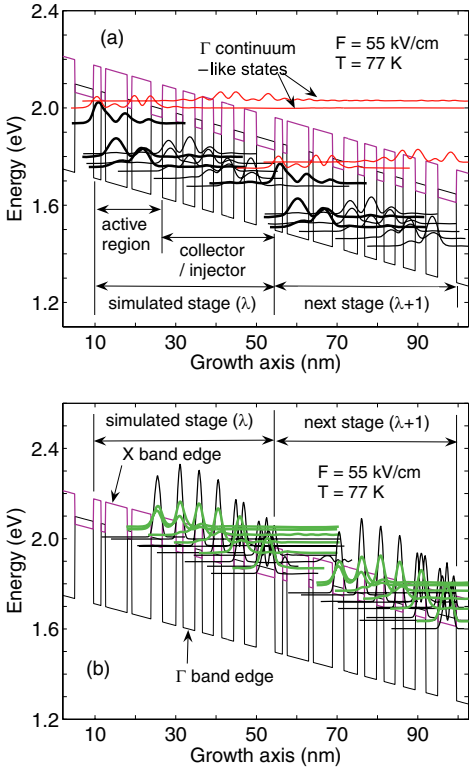

Fig. 1 (a) Energy levels and wave function moduli squared of ten Γ-valley subbands in two adjacent stages for the 45% QCL [1]. The bold black lines in each stage represent the lasing action levels, and the top two red thin lines are the Γ-valley continuum-like states. (b) Energy levels and wave function moduli squared of nine longitudinal X states (thin black lines) and six transverse X subbands (bold green lines) in two adjacent stages for the 45% QCL

Table 1 Scattering mechanisms included in the Monte Carlo model for the Γ- and X-valley states

Γ valley	X1 valley	X2 valley
electron-LO	electron-LO	electron-LO
electron-electron		
Γ →X1	X1→ Γ	X2→ Γ
Γ →X2	X1→X2	X2→X1
		X2→X2

threshold field) and $T = 77$ K. Ten important Γ-valley subbands in each stage are employed in the Monte Carlo model, with the highest two subbands being the continuum-like states considered in Ref. [3]. The number of X states in each stage is the same and chosen so that the highest X subband is right above the second Γ continuum-like state and below other higher X levels. At $F = 55$ kV/cm and $T = 77$ K, nine longitudinal and six transverse X-valley subbands satisfy this rule and are used in the simulation.

The various scattering mechanisms included in the Monte Carlo simulation are listed in Table 1. The intervalley scattering mechanism is written in the form of A→B (e.g., Γ →X1) in the table, with A being the initial valley and B the final valley. The electron-LO-phonon scattering is included for all the valleys, but the electron-electron (e-e) interaction is implemented only for the Γ-valley states, since the electron density in the X valleys should be low for an operational QCL structure under typical current densities. The intervalley scattering X2 → X2 takes place due to the double-degeneracy of the X2-valley states. For all the scattering mechanisms, we include both the intrastage and interstage scattering events, with the latter yielding the current flow through the QCL. The electron-phonon interaction (electron-LO and intervalley scattering) is implemented assuming bulk phonons and quasi-2D electrons. The binary quasi-2D e-e scattering is included into the Monte Carlo simulation by employing the quasistatic multisubband screening model [13,14]; the antiparallel-spin and parallel-spin e-e collisions are both taken into account, with the exchange effect included for the parallel-spin e-e scattering [15,16].

The possible interstage scattering events of the simulated stage λ are sketched in Fig. 2. Due to the translational symmetry of QCL structures, we are allowed to simulate the carrier transport over a central stage λ within the charge-conserving scheme [7]. Each time a carrier in a state $|\,\mathbf{k}, \nu_\ell \lambda \ell\rangle$ undergoes an interstage scattering process to a new state $|\,\mathbf{k}', \nu'_\ell(\lambda \pm 1)\ell'\rangle$ (i.e., processes ② and ③), it is properly reinjected into the central region by the corresponding processes ① and ④, respectively, so that the number of carriers in the simulated stage λ is conserved.

The current density J across the whole device is defined in terms of the carrier flux exiting the simulated λth stage

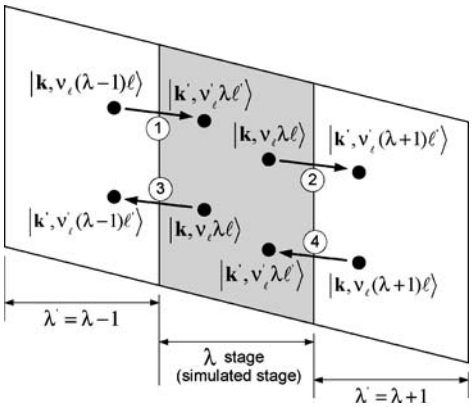

Fig. 2 Schematic of the interstage scattering processes for the 45% QCL under an applied field

across its left and right boundaries [8]:

$$J \propto \sum_{\mathbf{k},\mathbf{k}'} \sum_{\nu_\ell,\nu'_\ell} \sum_{\ell,\ell'} \left[P_{\mathbf{k},\nu_\ell\lambda\ell;\mathbf{k}',\nu'_\ell(\lambda+1)\ell'} f_{\mathbf{k},\nu_\ell\lambda\ell} - P_{\mathbf{k},\nu_\ell\lambda\ell;\mathbf{k}',\nu'_\ell(\lambda-1)\ell'} f_{\mathbf{k},\nu_\ell\lambda\ell} \right]. \quad (2)$$

Hence, the current density J can be obtained by counting the interstage scattering processes. Furthermore, the transition rates for processes ② and ③ can be regarded as the same as those of processes ① and ④, respectively, thanks to the translational symmetry. As a benefit of this equivalence, we only need to solve for the states of two full adjacent stages to compute all the interstage transition rates.

3 Numerical results and discussion

Figure 3 shows the applied field vs. current density characteristics for the 45% QCL at 77 K and 300 K, with and without the X-valley transport included. The simulated threshold current density J_{th} ($F = 48$ kV/cm) with the

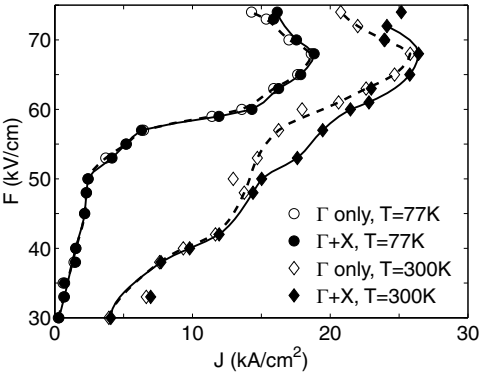

Fig. 3 Electric field vs. current density characteristics for the 45% QCL at $T = 77$ K and $T = 300$ K, with and without the X-valley transport included

X-valley transport included is 2.28 kA/cm^2 at $T = 77$ K, in qualitative agreement with the experiment ($J_{th} \approx 4$ kA/cm^2), and 14.39 kA/cm^2 at room temperature, in excellent agreement with the experiment ($J_{th} = 15$ kA/cm^2) [1]. At a low temperature (77 K), the inclusion of X-valley transport has negligible effect on the current density up to very high fields (above 65 kV/cm). At room temperature, the increase in current density due to the X-valley leakage is appreciable, provided that the applied field is above the threshold field of 48 kV/cm, because the Γ-X intervalley scattering becomes strong owing to many more active intervalley phonons.

However, the overall effect of the X-valley leakage on the current density is small at both temperatures for the 45% QCL, as explained in the following. The carrier loss to the X valley happens mainly through two channels: the first one is due to the coupling (electronic wavefunction overlap) of the Γ-valley continuum-like states with the X-valley states in the same stage, while the second one is due to the coupling of the Γ-valley localized states in the simulated stage with the X-valley states in the next stage. The wavefunction overlap responsible for these two channels can be seen in Fig. 1. The two channels both lead to the reduction of electron population in the Γ valley, nevertheless, only the second channel directly affects the current density. The 45% QCL was designed to have a high barrier height (359 meV) in the Γ valley, so that the Γ-valley states would be well localized, resulting in less thermal excitation to the Γ continuum-like states in the simulated stage, and a very small overlap with the X states in the next stage. Therefore, the effect of the X-valley leakage on the current density is not pronounced in the 45% QCL case at both cryogenic and room temperatures, giving rise to the superior performance of the device. In contrast, the effect is significant in the 33% QCL case, especially at high fields and high temperature [9], which is a likely explanation of why the 33% structure did not achieve lasing action at room temperature.

4 Conclusion

We have presented the first Monte Carlo simulation incorporating the effects of the X-valley leakage on the operation of GaAs-based QCLs. The simulated threshold-current density with the X-valley transport included is in very good agreement with experiment at cryogenic and room temperatures for the 45% QCL. Carrier loss to the X valley occurs due to the coupling of the Γ continuum-like states with the X states in the same stage, and due to the coupling between the Γ localized states in the simulated stage with the X states in the next stage. The effect of the X-valley leakage on the current density is small for the 45% QCL, thanks to the excellent confinement of the Γ states. This realistic simulator can also be adapted to account for the indirect-valley leakage in InP-based structures, thereby becoming a versatile aid in the design of mid and far-infrared QCLs.

Acknowledgments We would like to thank Dr. Stephen Goodnick for his help regarding the electron-electron interaction. This work was supported by the Wisconsin Alumni Research Foundation (WARF).

References

1. Page, H., et al.: Appl. Phys. Lett. **78**, 3529 (2001)
2. Sirtori, C., et al.: Appl. Phys. Lett. **73**, 3486 (1998)
3. Indjin, D., et al.: Appl. Phys. Lett. **81**, 400 (2002)
4. Wilson, L.R., et al.: Appl. Phys. Lett. **76**, 801 (2000)
5. Mermelstein, C., et al.: Proc. SPIE **5738**, 13 (2005)
6. Indjin, D. et al.: J. Appl. Phys. **91**, 9019 (2002)
7. Iotti, R.C., Rossi, F.: Phys. Rev. Lett. **87**, 146603 (2001)
8. Iotti, R.C., Rossi, F.: Rep. Prog. Phys. **68**, 2533 (2005)
9. Gao, X., Botez, D., Knezevic, I.: Appl. Phys. Lett. **89**, 191119 (2006)
10. Mircetic, A., et al.: J. Appl. Phys. **97**, 084506 (2005)
11. Jovanovic, V.D., et al.: Appl. Phys. Lett. **86**, 211117 (2005)
12. Vinter, B.: Phys. Rev. B **66**, 045324-1 (2002)
13. Goodnick, S.M., Lugli, P.: Phys. Rev. B **37**, 2578 (1988)
14. Dur, M., et al.: Phys. Rev. B **54**, 17794 (1996)
15. Moško, M., et al.: Phys. Rev. B **51**, 16860 (1995)
16. Mošková, A., Moško, M.: Phys. Rev. B **49**, 7443 (1994)